

Article

# On C-Band Quad-Polarized Synthetic Aperture Radar Properties of Ocean Surface Currents

Shengren Fan <sup>1</sup> , Vladimir Kudryavtsev <sup>2,3</sup>, Biao Zhang <sup>1,4,\*</sup> , William Perrie <sup>5</sup>, Bertrand Chapron <sup>2,6</sup> and Alexis Mouche <sup>6</sup> 

<sup>1</sup> School of Marine Sciences, Nanjing University of Information Science & Technology, Nanjing 210044, China; sr\_fan@nuist.edu.cn

<sup>2</sup> Russian State Hydrometeorological University, St. Petersburg 195196, Russia; kudr@rshu.ru (V.K.); bertrand.chapron@ifremer.fr (B.C.)

<sup>3</sup> Marine Hydrophysical Institute, Sevastopol 299011, Russia

<sup>4</sup> Southern Marine Science and Engineering Guangdong Laboratory, Zhuhai 519082, China

<sup>5</sup> Bedford Institute of Oceanography, Fisheries and Oceans Canada, Dartmouth, NS B2Y 4A2, Canada; william.perrie@dfo-mpo.gc.ca

<sup>6</sup> Laboratoire d'Océanographie Physique Spatiale, Ifremer, Brest 29200, France; alexis.mouche@ifremer.fr

\* Correspondence: zhangbiao@nuist.edu.cn; Tel.: +86-25-58695692

Received: 1 September 2019; Accepted: 2 October 2019; Published: 5 October 2019



**Abstract:** We present new results for ocean surface current signatures in dual co- and cross-polarized synthetic aperture radar (SAR) images. C-band RADARSAT-2 quad-polarized SAR ocean scenes are decomposed into resonant Bragg scattering from regular (non-breaking) surface waves and scattering from breaking waves. Surface current signatures in dual co- and cross-polarized SAR images are confirmed to be governed by the modulations due to wave breaking. Due to their small relaxation scale, short Bragg waves are almost insensitive to surface currents. Remarkably, the contrast in sensitivity of the non-polarized contribution to dual co-polarized signals is found to largely exceed, by a factor of about 3, the contrast in sensitivity of the corresponding cross-polarized signals. A possible reason for this result is the co- and cross-polarized distinct scattering mechanisms from breaking waves: for the former, quasi-specular radar returns are dominant, whereas for the latter, quasi-resonant scattering from the rough breaking crests governs the backscatter intensity. Thus, the differing sensitivity can be related to distinct spectral intervals of breaking waves contributing to co- and cross-polarized scattering in the presence of surface currents. Accordingly, routinely observed current signatures in quad-polarized SAR images essentially originate from wave breaking modulations, and polarized contrasts can therefore help quantitatively retrieve the strength of surface current gradients.

**Keywords:** quad-polarized SAR; ocean surface current; polarization decomposition; Bragg scattering; breaking waves

## 1. Introduction

With the advent of new spaceborne synthetic aperture radar (SAR) systems, more detailed information on the ocean surface signatures of high-resolution ocean–atmosphere processes is becoming available. Due to their high spatial resolution, wide swath acquisitions, and their capability to operate at day and night over the global ocean, C-band spaceborne SAR microwave sensors can often capture spectacular manifestations of mesoscale and submesoscale ocean surface signatures. Surface floating buoys (drifters) and shipborne marine radar can measure near-surface currents [1,2], with the former only able to measure current velocities at depths of about 15 m, and the latter is limited by the detection

range, which is rather short, about 4 km. Though high-frequency (HF) radar is capable of remotely sensing the ocean surface current field, with large coverage, the retrieval process is complicated because the currents contain contributions from the wave-induced Stokes drift [3,4]. In any case, it has been demonstrated that single- and dual-antenna SARs have the capability to measure line-of-sight or vector currents [5–8]. Since the RADARSAT-2 (RS-2) launch in 2007, more than a decade of quad-polarized SAR images are readily available. This helps to advance the interpretation and quantification of various ocean surface phenomena (e.g., currents, sea surface thermal fronts, and oceanic internal waves) as well as to better understand the microwave scattering from the ocean surface.

Compared to optical observations [9,10], the diversity of radar polarization observations can provide further help to better isolate the measured roughness variations between the changes of polarized resonant Bragg scatters and non-polarized scatters associated with breaking waves. Previous studies have revealed that a ‘conventional’ simple model based on Bragg scattering dramatically underestimates the observed radar signatures of ocean currents [11]. The reason is that the relaxation rate of short Bragg waves is very fast and these waves are therefore not modulated by typical current gradients, which have a width of the order of 1 km. Radar imaging models have been improved following the integral equation method [12] and the composite surface Bragg theory [13,14]. By inclusion of intermediate scale waves carrying the shorter Bragg waves, the gap between simulated and observed radar backscatter anomalies has been reduced, but still the discrepancy exists [15,16].

Previous investigation suggested that the effect of wave breaking on radar scattering might provide the explanation for this discrepancy, between simulated and observed radar signatures of ocean currents [17]. In particular, wave-current interactions amplify wave breaking dissipation which in turn results in an enhancement of shorter gravity waves, including Bragg waves [18]. Accordingly, wave breaking effects [19] should be taken into account when simulating radar returns in areas of strong currents [20,21]. Wave breaking statistics can be based on the threshold level approach [22], and the relaxation-type wave-current interactions model [23]. The crucial role of wave breaking in radar imaging of ocean currents has been further demonstrated on the basis of previously developed models [17]; as well as dual co- and cross-polarized SAR observations of meso-scale currents and internal waves [9,10,24,25], nonlinear Ekman divergence [26] and sea surface temperature front signatures [27].

As already suggested [17,28] and tested [24,29,30] for particular case-studies, an effective methodology can build on previous work that uses the dual co-polarization (VV and HH) radar data to quantitatively assess contributions of Bragg and non-Bragg scattering (associated with wave breaking) in SAR imaging of different ocean surface phenomena, such as surface slicks, current gradients, and wind field features. Recently, using a large number of RS-2 quad-polarized SAR measurements, the contribution of wave breaking to C-band dual co-polarized scattering has been quantified under different incidence angles and wind conditions [31]. Results show that cross-polarized scattering from breaking waves can reach 80% of the total normalized radar cross-section (NRCS) for wind speeds up to 20 m/s, which suggests that wave breaking can play a crucial role in cross-polarized radar imaging of the ocean current, like co-polarization.

In this paper, we consider six particular cases of RS-2 quad-polarized SAR images to further precisely identify whether the short Bragg waves, or the modulations of wave breaking, are the most sensitive to the presence of ocean surface features (ocean currents, internal waves and fronts). Moreover, we further explore and analyze the differing sensitivity between co- and cross-polarized signals to breaking wave modulations. This paper is organized as follows. The description of the SAR data and the radar imaging properties are presented in Section 2.1. In Section 2.2, the decomposition method is introduced. In Section 3, we present the analyses of different ocean surface features, followed by a corresponding discussion in Section 4. Conclusions are given in Section 5.

## 2. Data and Model Approach

### 2.1. Data

In a recent study, the background properties, in particular, the dependence of wave breaking contributions in dual co- and cross-polarized SAR signals on incidence angle, azimuth and wind speed, have been reported [31]. In the present study, we investigate the quad-polarized SAR signatures of meso-scale ocean phenomena which have been visually detected in available RS-2 SAR scenes.

In total, 71 SAR images contain distinct signatures of surface currents, natural slicks, ocean fronts and internal waves (IWs). Hereafter, we concentrate the analysis on six “typical” quad-polarized SAR images, acquired over the Aleutian Islands, on 13:53 UTC, 24 May 2012 (see Figure 1), on 14:35 UTC, 15 August 2009 (see Figure 3) on 22:07 UTC, 18 March 2009 (see Figure 5), on 21:30 UTC, 26 April 2009 (see Figure 7), on 01:57 UTC, 9 August 2009 (see Figure 9), and on 18:20 UTC, 14 September, 2009 (see Figure 11). These SAR scenes provide quite generic environmental conditions to analyze and discuss the main mechanisms responsible for the manifestation of ocean and atmospheric processes, as detected at the ocean surface. The RS-2 fine quad-polarization imaging mode provides SAR images in HH- ( $\sigma_0^{hh}$ ), VV- ( $\sigma_0^{vv}$ ) and cross-polarized (CP) polarizations, defined as  $CP = (\sigma_0^{vh} + \sigma_0^{hv})/2$ . For these six cases, the HH polarization scenes are shown in Figures 1a, 3a, 5a, 7a, 9a and 11a. It should be noted that the noise-equivalent sigma-zero (NESZ) is very low for the quad-polarization imaging mode with approximate values of  $-36.5 \pm 3$  dB [32]. The NESZ has been subtracted from co- and cross-polarized NRCS before the polarimetric analysis.

In Figure 1, periodic bright/dark signatures are well expressed in HH and  $PR = \sigma_0^{hh}/\sigma_0^{vv}$  images. This case, which is only VV, has previously been considered [33] in the context of developing an improved C-band SAR GMF for ocean surface wind speed retrieval. It was reported that the observed periodic features are caused by near-surface wind oscillations induced by atmospheric gravity waves. Figure 3a,b depicts SAR signatures of IWs: periodic dark and bright oscillatory patterns are related to the typical manifestations of IWs trains. The other linear feature is considered to be a solitary IW. The unique step-like change of the HH-signal, displaying a bright linear feature around the front in Figure 5a,b, is presumably associated with the modulation of the near-surface winds over the SST front and convergence of the current around the frontal line. Figures 7a, 9a and 11a, and the ‘number 2’ feature in Figure 3a exhibit very different bright linear signatures which are quite visible in HH-polarized images, and in processed PR images, which can be further interpreted as manifestations of the surface current boundaries.

### 2.2. Model Approach

To interpret these observed high-resolution SAR features, we follow the approach suggested in [29] and further extended to CP in [24,30,31]. Following this approach, VV and HH normalized radar cross sections (NRCSs) can be separated into two parts, associated with the polarized resonant Bragg scattering  $\sigma_{OB}^{pp}$  and the non-polarized (NP) radar returns from breaking waves  $\sigma_{wb}$ :

$$\sigma_0^{pp} = \sigma_{OB}^{pp} + \sigma_{wb} \quad (1)$$

Equation (1) is then solved to derive the NP contribution,  $\sigma_{wb}$ , from the dual co-polarized NRCS measurements:

$$\sigma_{wb} = \sigma_0^{vv} - \Delta\sigma_0 / (1 - p_B) \quad (2)$$

where  $\Delta\sigma_0 = \sigma_0^{vv} - \sigma_0^{hh}$  is the polarization difference (PD), and  $p_B$  is the estimated polarization ratio (PR) based on the two-scale Bragg scattering model (TSM) (see Figure 1a in [31]).

CP NRCS can also be decomposed into two parts,

$$\sigma_0^{vh} = \sigma_{OB}^{vh} + \sigma_{wb}^{vh} \quad (3)$$

where  $\sigma_{0B}^{vh}$  is estimated Bragg scattering for CP from TSM, and  $\sigma_{wb}^{vh}$  corresponds to the contribution of wave breaking to CP, defined as [31]:

$$\sigma_{wb}^{vh} = \sigma_0^{vh} - r_B \Delta \sigma_0 \quad (4)$$

where  $r_B$  is the TSM estimate for CP-over-PD ratio:  $r_B = \sigma_{0B}^{vh} / \Delta \sigma_0$  (see Figure 3a in [31]). Hereafter the contribution of wave breaking to CP, (4), is denoted CPwb. Detailed description of the relative contribution of wave breaking to dual co- and cross-polarized NRCS can be found in [31].

Following Equations (1) and (3), the original dual co- and cross-polarized images are thus transformed into new images which possess information on very different radar scattering mechanisms: Bragg scattering (associated with PD) provided by the fast-response of short wind waves, and the contributions of wave breaking to dual co- and cross-polarized NRCS, as defined by Equations (2) and (4), respectively. Anticipating the different sensitivities of short wind waves and wave breaking to various ocean phenomena, this set of new images can then serve as an effective way to interpret the original SAR data. The definition of the key parameters used in this paper are shown in Table 1.

**Table 1.** Definition of the key parameters.

PR	$\sigma_0^{hh} / \sigma_0^{vv}$
PD	$\sigma_0^{vv} - \sigma_0^{hh}$
NP	$\sigma_0^{vv} - \Delta \sigma_0 / (1 - p_B)$
CP	$(\sigma_0^{vh} + \sigma_0^{hv}) / 2$
CPwb	$\sigma_0^{vh} - r_B \Delta \sigma_0$
$p_B$	$\frac{ G_{hh} ^2}{ G_{vv} ^2} \cdot \frac{1 + g_{hh} \cdot s_i^2}{1 + g_{vv} \cdot s_i^2}$
$r_B$	$\frac{ G_{vv} - G_{hh} ^2}{ G_{vv} ^2 -  G_{hh} ^2} \cdot \frac{s_n^2}{\sin^2 \theta}$
contrast	$(y - \bar{y}) / \bar{y}$

Note:  $G_{hh}$ ,  $G_{vv}$ ,  $g_{hh}$ , and  $g_{vv}$  are scattering coefficients of TSM defined by Equations (A2) and (A3) in [31],  $s_i^2$  and  $s_n^2$  are the mean square slope (MSS) of tilting waves, in and out of the direction of the incidence plane.

In the following Section, SAR observations of several different ocean surface features (e.g., atmospheric gravity waves, oceanic internal waves, sea surface temperature (SST) fronts, and ocean currents) will be assessed. Specifically, we estimate different polarized images (PR, NP, PD, and CPwb) and use them to identify these phenomena. They will be individually investigated beginning with an atmospheric gravity wave, followed by Figures 1 and 2; oceanic internal waves, followed by Figures 3 and 4; SST fronts, followed by Figures 5 and 6; ocean currents, followed by Figures 7 and 8, Figures 9 and 10, and Figures 11 and 12.

### 3. Scattering Signatures

#### 3.1. Atmospheric Gravity Waves

The case shown in Figure 1 provides quad-polarized SAR signatures of wind speed oscillations induced by atmospheric gravity waves. This case had been used [33] to test the capability of a new C\_SARMOD2 GMF to retrieve wind speed variability from VV-polarized SAR data. In our present case, the full set of quad-polarized SAR images, and their companions, PD, NP, CPwb, and PR = HH/VV, are used. As obtained, the bright/dark features are quite visible in HH and PR: the larger the wind speed, the larger is PR. Such behavior presumes that the wind sensitivity of NP (wave breaking) is higher than the wind sensitivity of Bragg waves. This result can also be shown to occur using the image contrast,  $k_y = (y - \bar{y}) / \bar{y}$ , defined as the deviation from the mean value scaled by the mean, of NP, PD, CPwb. As obtained, the intensities of NP- and CPwb contrast are much higher than the intensities of the PD contrast.

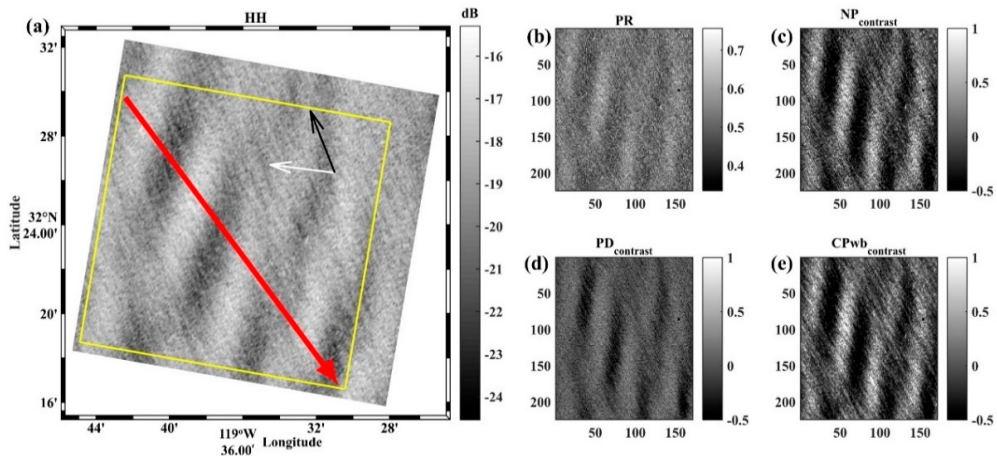


**Figure 1.** Synthetic aperture radar (SAR) images containing atmospheric gravity waves: (a) RS-2 SAR HH-polarized images (dB units) of an area of the West Coast of USA acquired at 13:53 UTC on May 24, 2012. The key parameters associated with the enlarged region of the yellow fragment in (a) are estimated as: (b) polarization ratio (PR) (linear units); (c) non-polarized (NP) contrast; (d) polarization difference (PD) contrast, and (e) cross-polarized wave breaking (CPwb) contrast. The incidence angle, averaged wind speed and the angle between radar look direction and wind direction are about 44 degrees, 11 m/s and 59 degrees, respectively. The black and white arrows in (a) correspond to wind direction and radar look direction. Wind direction is from the NDBC buoy, wind speed from the C\_SARMOD2 GMF. RS-2 data are a product of MacDonald, Dettwiler, and Associates, Ltd. All rights reserved.

Transects of PR, NP contrast, PD contrast, and CPwb contrast, along the red arrow in the yellow fragment shown in Figure 2a-d correspondingly, further clearly indicate that the wind sensitivity of the NRCS components supported by wave breaking is indeed stronger than that of PD associated with Bragg scattering. Note that Figure 2b,d show that the transects of NP and CPwb contrasts are very similar. The wind sensitivity to the wave breaking contribution to co- and cross-polarized signals is thus similar, confirming previously reported results ([31], their Figure 4). As shown in Figure 2b,c, the scale of NP contrast is about twice that of PD contrast. NP (wave breaking) is thus more sensitive to wind speed variations than PD (short-scale Bragg waves), which is also consistent with previously reported results ([24], compare their Figure 5b and Figure 12b).

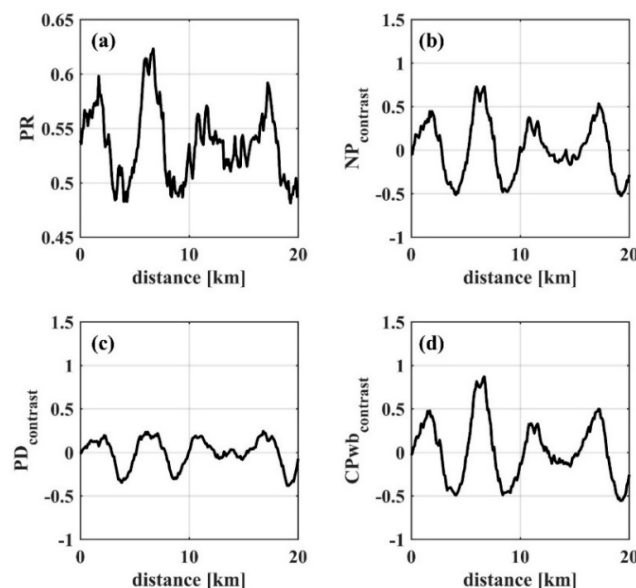


**Figure 2.** Transects across the atmospheric gravity waves along the red arrow shown in Figure 1a: (a) PR, (b) NP contrast, (c) PD contrast, (d) CPwb contrast.

### 3.2. Oceanic Internal Waves

The manifestation of oceanic IWs in SAR images is shown in Figure 3. Firstly, the train of short-period IWs is easily recognized, in the first yellow fragment of plot (a) (marked by fragment #1). Another second feature, which may be treated as SAR signatures of solitary IWs, with a corresponding bright linear feature, spreads from top to bottom of the HH image (marked by fragment #2). Enlarged fragments of IWs manifestations in PR-, NP-, PD-, and CPwb-components of quad-polarized SAR images are shown in plots (3b) to (3e) (for IWs train) and in plots (3f) to (3i) (for the solitary IW). Firstly, we notice that modulations are well expressed in PR, for either or both type of IWs. This again indicates that modulations of NP components exceed the modulations due to Bragg scattering. This observation is verified by considering the modulations of NP- and PD-signals, e.g. compare plots (3c) and (3d) for IW train and plots (3g) and (3h) for the solitary IW. For both cases, the modulations of the PD signal are not detectable whereas NP modulations are quite well expressed. Secondly, similar to NP, modulations of the CPwb-signal are also visually detectable, but less pronounced.

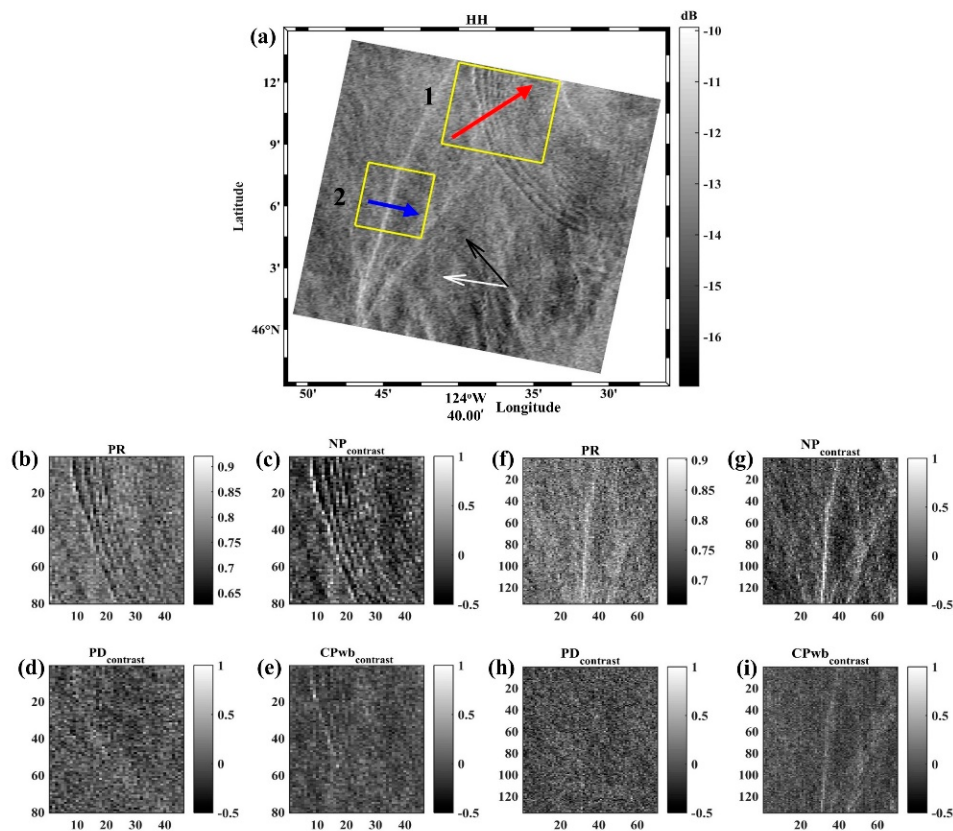


**Figure 3.** SAR images containing a oceanic internal solitary wave (IW) and a train of IWs: (a) RS-2 SAR HH-polarized images (dB units) of an area of the West Coast of USA acquired at 14:35 UTC on August 15, 2009. The key parameters associated with the enlarged region of the yellow fragment in (a) are estimated as: (b,f) PR (linear units); (c,g) NP contrast; (d,h) PD contrast; (e,f) CPwb contrast. The incidence angle, averaged wind speed and the angle between radar look direction and wind direction are about 29 degrees, 6 m/s and 39 degrees, respectively. RS-2 data are a product of MacDonald, Dettwiler, and Associates, Ltd. All rights reserved.

Transects over the IW train and the solitary IW (red and blue arrows) are shown in Figure 4a,d,e,h, correspondingly. As already noticed, for both cases, the strongest modulations are observed in the NP signal, whereas modulations in CPwb are also observed but are not prominent, and modulations of the PD signal associated with Bragg scattering modulations are negligible, and thus not detectable by a C-band SAR.

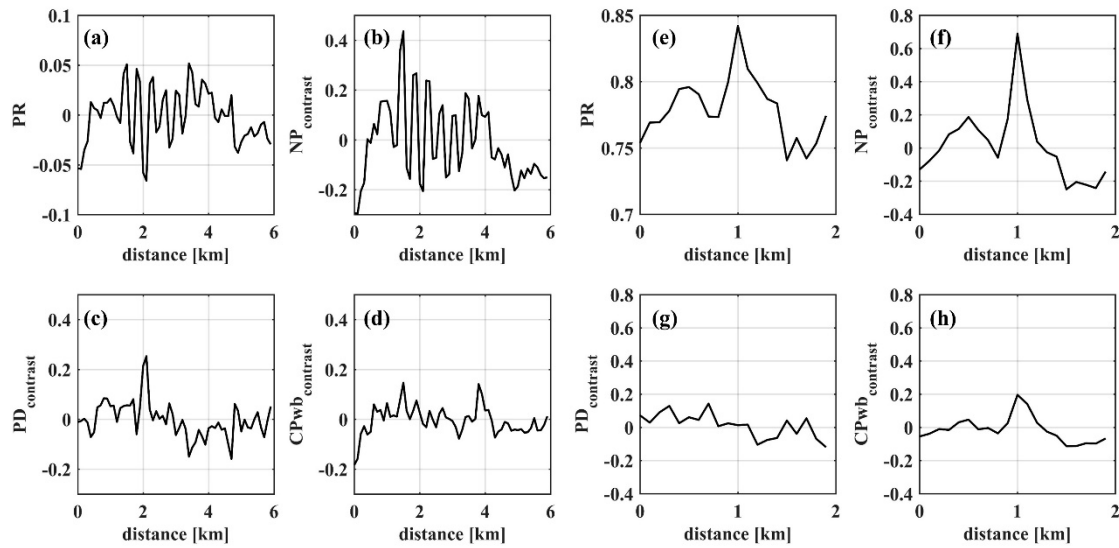


**Figure 4.** Transects across the IW train along the red arrow shown in Figure 3a: (a) PR, (b) NP contrast, (c) PD contrast, (d) CPwb contrast. Transects across the solitary IW along the blue arrow shown in Figure 3a: (e) PR, (f) NP contrast, (g) PD contrast, (h) CPwb contrast.

### 3.3. SST Fronts

Figure 5 presumably provides the manifestation of an oceanic temperature front. A step-like change of HH signal in the direction of the yellow fragment is likely caused by the effect of the atmospheric boundary layer transformation over the temperature front. As known and often reported [17,34,35], the spatial variations of the SST alter stratification of the marine atmospheric boundary layer (MABL) and subsequently the surface wind stress. In our case, wind stress and the near-surface wind speed (and consequently NRCS) over the cold side of the front decrease relative to the wind speed over the warm side. This wind field feature leads to coherent step-like changes of the PR, NP-, PD- and CPwb-contrast over the front, as well expressed in Figure 5.

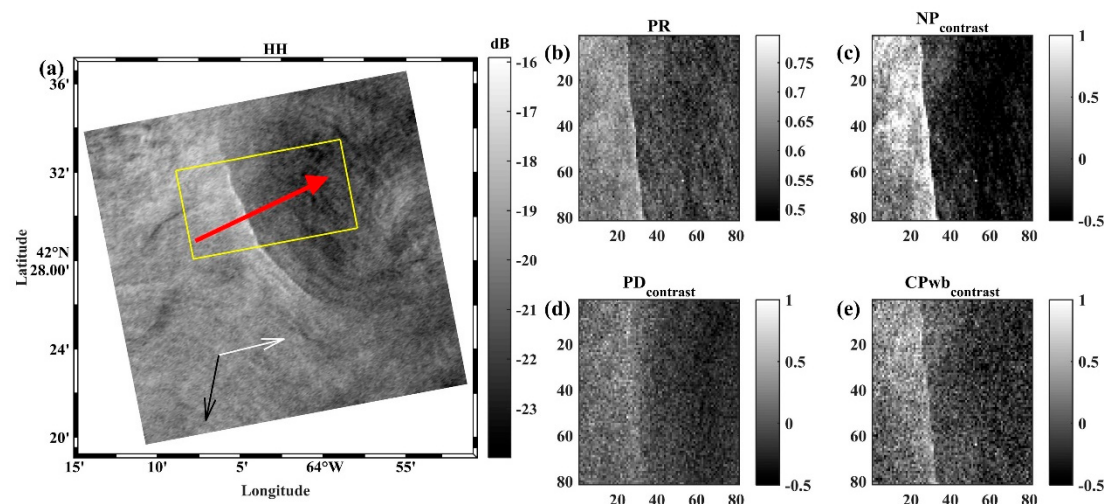


**Figure 5.** SAR images containing sea surface temperature (SST) front: (a) RS-2 SAR HH-polarized images (dB units) of an area of the East Coast of USA acquired at 22:07 UTC on March 18, 2009. The key parameters associated with the enlarged region of the yellow fragment in (a) are estimated as: (b) PR (linear units); (c) NP contrast; (d) PD contrast, and (e) CPwb contrast. The incidence angle, averaged wind speed and the angle between radar look direction and wind direction are about 33 degrees, 4 m/s and 112 degrees, respectively. RS-2 data are a product of MacDonald, Dettwiler, and Associates, Ltd. All rights reserved.

There is also a noticeable bright line in the PR image that follows the SST frontal line. A possible origin of this bright PR feature can be interpreted as a result of the local enhancement of wave breaking and consequently NP radar component (Figure 5c). This area of enhanced wave breaking traces the surface current convergence at the edge of the SST front [10,24]. Surprisingly, modulations of CPwb around the front are much weaker than NP, though both signatures originate from the same surface phenomenon—local wave breaking enhancement. Finally, modulations of PD around the front are weak and almost negligible.

Figure 6b–d display the transects of NP, PD and CPwb contrasts along the red arrow in Figure 5a. Each of the transects exhibits step-like changes related to the near-surface wind speed change over the SST front. In addition, as mentioned above, NP exhibits a strong peak value around the front, whereas in the CP signal, this is less pronounced, and almost negligible in PD signal. Therefore, we conclude that the modulation of the wave breaking by the surface currents dominates the co-polarized SAR image contrasts, and the effect of Bragg resonant scattering on SAR image contrasts is negligible.

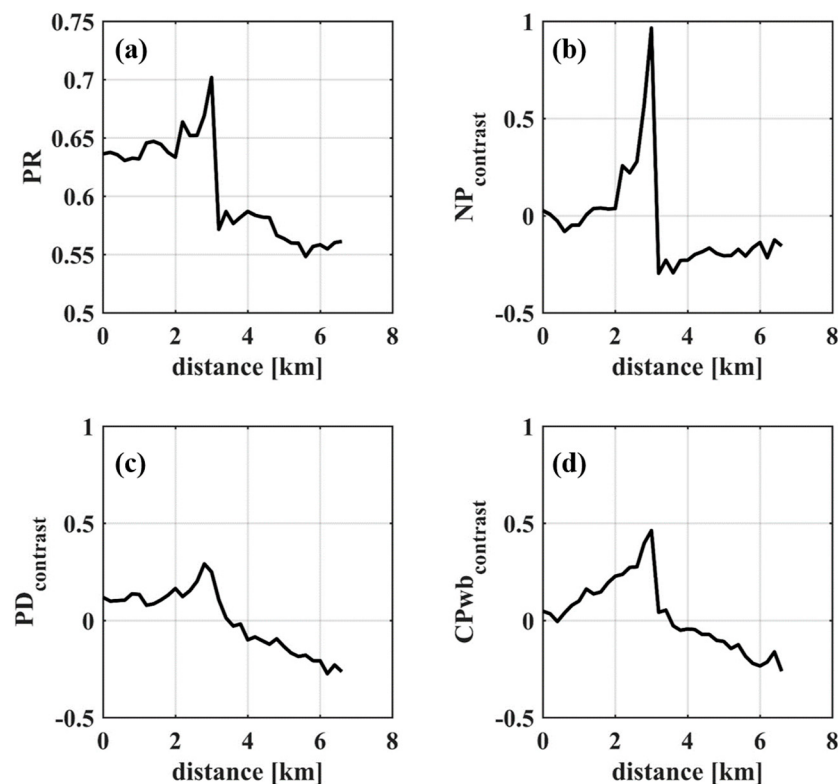


**Figure 6.** Transects across the SST front along the red arrow shown in Figure 5: (a) PR, (b) NP contrast, (c) PD contrast, (d) CPwb contrast.

### 3.4. Ocean Currents

Figure 7 illustrates specific features of a surface current. Again, bright linear features, well delineated in the HH image, trace the ocean surface current boundary (front). Enlarged fragments of this typical SAR signature are shown in plots (7b) to (7e) to reveal the following: the current boundary is well expressed in PR, plot (7b), suggesting that modulation of wave breaking (NP-signal) should again be much stronger than modulations associated with resonant Bragg waves; this is confirmed with plots (7c) and (7d) illustrating strong modulations of NP and negligible modulations of the PD, correspondingly; breaking wave modulations lead to measurable but smaller (as compare with NP) modulations in the CP signal, plot (7e).

These overall observations are confirmed by the transects shown in Figure 8. Well expressed peaks in PR and NP contrasts, around the current boundary, confirm the strong modulations of wave

breaking. Similar to the previous case, CPwb exhibits clear modulation, but this is not so well expressed when compared to NP-signal. Similar to the previous cases, the transect of PD contrast does not correlate with either NP or CPwb, confirming the absence of current impacts on short Bragg waves.

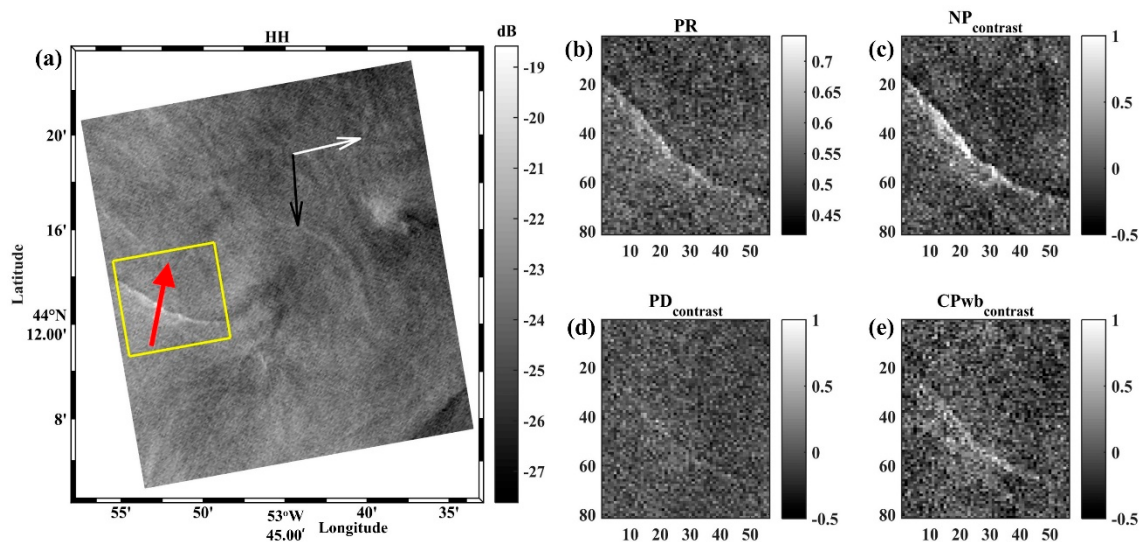


**Figure 7.** SAR images containing ocean current feature: (a) RS-2 SAR HH-polarized images (dB units) of an area of the East Coast of USA acquired at 21:30 UTC on April 26, 2009. The key parameters associated with the enlarged region of the yellow fragment in (a) are estimated as: (b) PR (linear units); (c) NP contrast; (d) PD contrast, and (e) CPwb contrast. The incidence angle, averaged wind speed and the angle between radar look direction and wind direction is about 39 degrees, 6 m/s and 96 degrees, respectively. RS-2 data are a product of MacDonald, Dettwiler, and Associates, Ltd. All rights reserved.

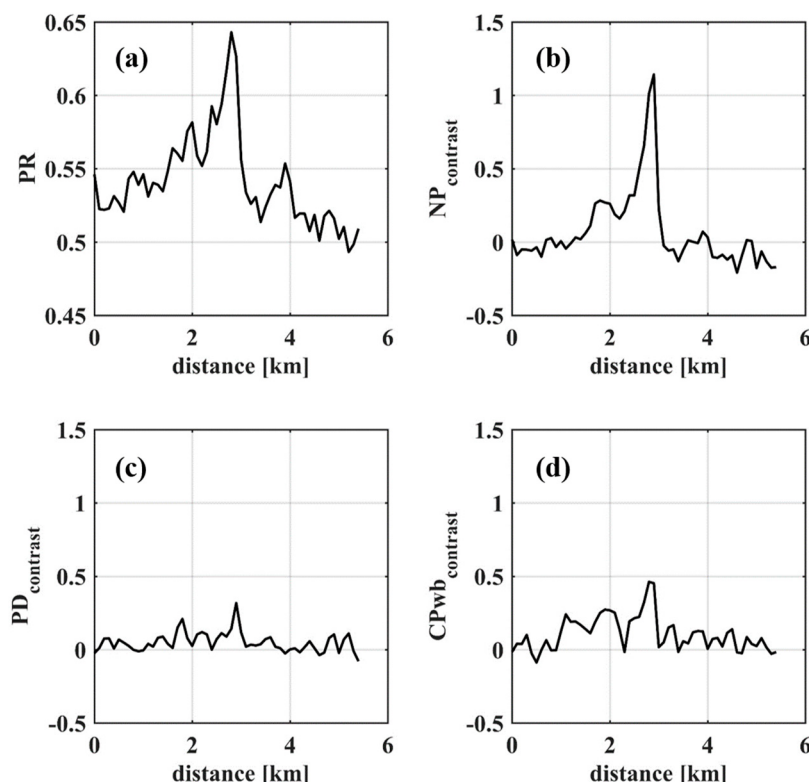


**Figure 8.** Transects across the current along the red arrow shown in Figure 7: (a) PR, (b) NP contrast, (c) PD contrast, (d) CPwb contrast.

Comparable to the case shown in Figure 7, Figure 9 illustrates another SAR signature of a surface current feature. Referring to Figure 9d, although this current feature is not visible in PD contrasts, it is quite well expressed in variations of NP and CPwb contrasts, Figure 9c,e. Quad-polarized SAR signatures of this current feature appear to systematically result from enhanced wave breaking, significantly contributing to NP and CPwb results.

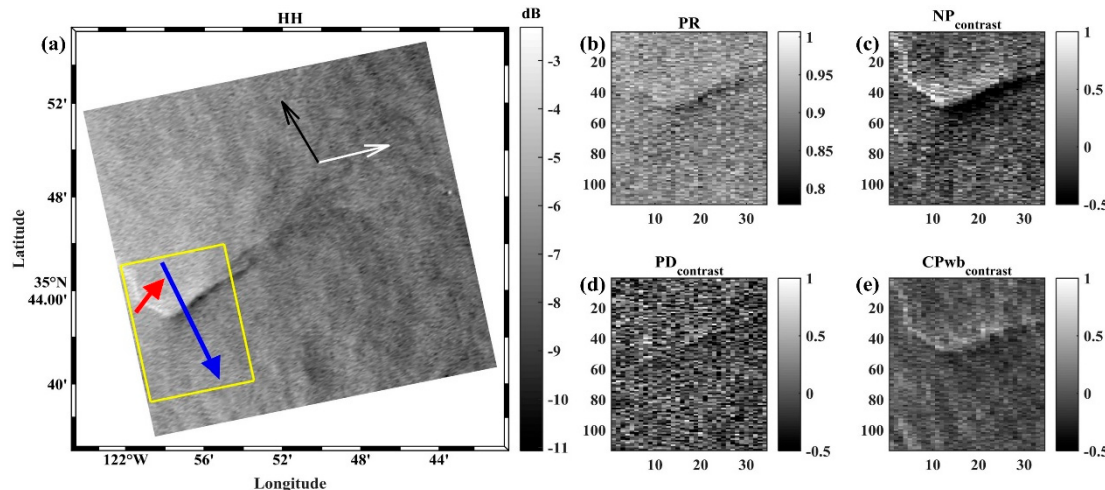


**Figure 9.** SAR images containing ocean current feature: (a) RS-2 SAR HH-polarized images (dB units) of an area of the West Coast of USA acquired at 01:57 UTC on August 9, 2009. The key parameters associated with the enlarged region of the yellow fragment in (a) are estimated as: (b) PR (linear units); (c) NP contrast; (d) PD contrast, and (e) CPwb contrast. The incidence angle, averaged wind speed and the angle between radar look direction and wind direction are about 23 degrees, 12 m/s and 108 degrees, respectively. RS-2 data are a product of MacDonald, Dettwiler, and Associates, Ltd. All rights reserved.

Transects shown in Figure 10 illustrate the profiles of PR, PD contrast, NP and CPwb contrasts along red and blue arrows in Figure 9a. The left two columns of transects in Figure 10 refer to the red arrow shown in Figure 9a, and the right two columns refer to the blue arrow. Along the two directions, distinct peaks of NP and CPwb contrasts are observed around the current boundary. PD variations are absent.

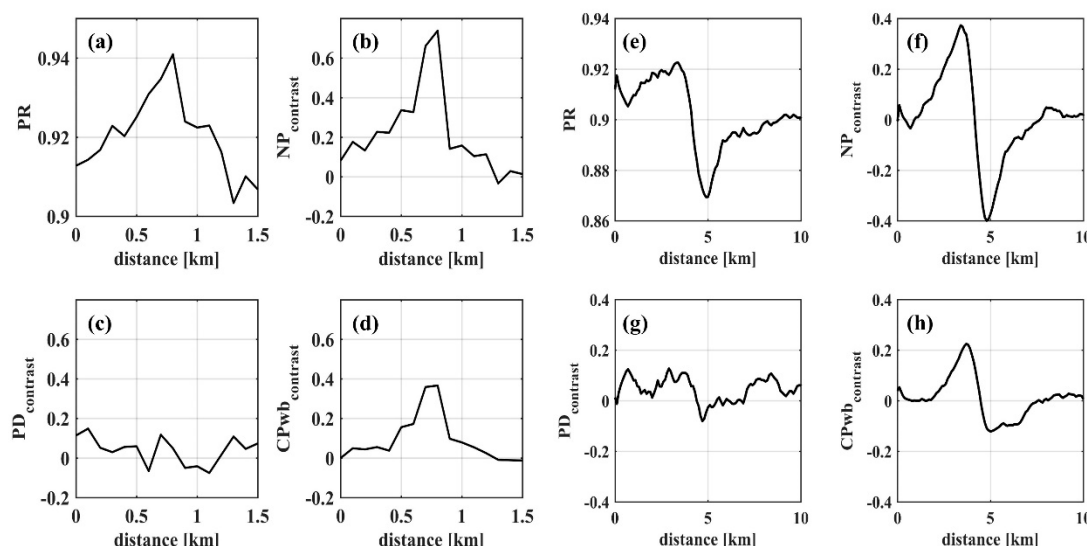


**Figure 10.** Transects across the current along the red arrow shown in Figure 9: (a) PR, (b) NP contrast, (c) PD contrast, (d) CPwb contrast. Transects across the current along the blue arrow shown in Figure 9: (e) PR, (f) NP contrast, (g) PD contrast, (h) CPwb contrast.

Figure 11 further displays another case of the SAR signature of a current feature. Similar conclusions can be drawn, with strong NP and CPwb image contrasts (Figure 11c,e). This result is furthermore supported by the PR image (Figure 11b), with larger PR values around the current which are well correlated with the enhanced NP component.

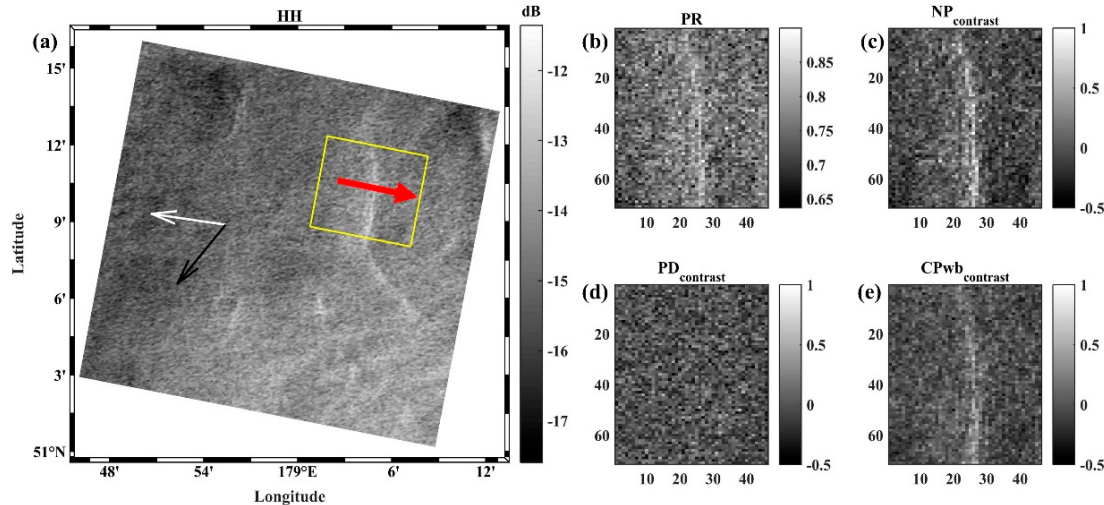


**Figure 11.** SAR images containing ocean current features: (a) RS-2 SAR HH-polarized images (dB units) of an area of the Aleutian Islands acquired at 18:20 UTC on September 14, 2009. The key parameters associated with the enlarged region of the yellow fragment in (a) are estimated as: (b) PR (linear units); (c) NP contrast; (d) PD contrast, and (e) CPwb contrast. The incidence angle, averaged wind speed and the angle between radar look direction and wind direction are about 34 degrees, 10 m/s and 60 degree, respectively. RS-2 data are a product of MacDonald, Dettwiler, and Associates, Ltd. All rights reserved.

#### 4. Discussion

Observations and results are summarized in Table 2. Modulations of PD, NP and CPwb signals caused by wind speed variability, due to either atmospheric gravity waves or atmospheric boundary layer transformation over the SST front, demonstrate the expected behavior imposed by the corresponding wind exponents reported in [31].

**Table 2.** Information on the SAR images and transects.

SAR Observation Time (UTC)	Feature	$\theta$ (deg)	$U_{10}$ (m/s)	$\Phi$ (deg)	$\frac{CP_{wb}}{NP}$	$R_1$	$\frac{PD}{NP}$	$R_2$
13:53, May 24, 2012	Atmospheric IWs	44	11	59	1.07	0.98	0.48	0.93
14:35, Aug 15, 2009	IW train	29	6	39	0.25	0.71	-0.05	-0.1
	solitary IW				0.35	0.96	0.06	0.19
22:07, Mar 18, 2009	SST front	33	4	112	0.39	0.95	0.33	0.92
21:30, Apr 26, 2009	current	39	6	96	0.36	0.79	0.17	0.69
01:57, Aug 9, 2009	current (red)	23	12	108	0.54	0.97	0.02	0.07
	current (blue)				0.42	0.92	0.02	0.07
18:20, Sept 14, 2009	current	34	10	60	0.55	0.85	-0.02	-0.07

Note:  $\Phi$  is radar look direction relative to the wind direction,  $R_1$  and  $R_2$  are correlation coefficients between  $CP_{wb}$  and  $NP$ , and  $PD$  and  $NP$ , respectively.  $\theta$ ,  $U_{10}$ , and  $\phi$  are radar incidence angle, wind speed at 10-m height and the angle between radar look direction and wind direction.

However, signatures of the ocean currents in the quad-polarized SAR images (and their derivatives, PR, PD, NP, and CPwb, see Table 1) are much more complicated. For C-band quad-polarized SAR measurements, surface currents have negligible impact on short resonant Bragg waves (PD-signal) which have small relaxation scale and thus do not “feel” the current. This result is in line with the previous research findings that any radar imaging model based on Bragg scattering theory dramatically underestimates observed SAR signatures of ocean currents [11,13,15,16].

In our study, additional experimental evidence is provided that the governing mechanism for radar imaging of ocean currents is the modulations of wave breaking. Significant contributions of wave breaking to co- and cross-polarized radar scattering (NP and CPwb signals in present notations) [31], result in quite well detected manifestations of the ocean current features in the SAR image, at arbitrary polarization configurations.

Unlike dual co-polarized SAR imaging, the manifestation of the current features in cross-polarized SAR images is not obvious and has rarely been reported [24,25]. However, the unexpected result found here is that the magnitudes of the current-induced contrasts in the NP-signal greatly exceed, by factors of 2-to-3, that in the CP-signal. This fact is rather puzzling because both non-polarized and cross-polarized scattering originate from precisely the same wave breaking events!

To interpret these quad-polarized SAR imaging peculiarities, we adopt the so-called relaxation approach to describe the wind wave transformation due to non-uniform currents. To that end, it is necessary to determine the spatial scales of the surface waves responsible for quad-polarized radar scattering and their differing surface current responses.

Firstly, the scale of Bragg waves, associated with the PD-signal from regular (non-breaking surface), is prescribed by the radar wavenumber,  $k_B$ , and may be expressed as  $k_B = 2k_R \sin\theta$ ; for C-band at moderate incidence angles, it is around 0.06 m. As already discussed, NP- and CPwb-signals are both associated with radar scattering from enhanced roughness at crests of breaking waves. The NP-signal is likely governed by quasi-specular radar returns from the roughness elements of large-scale breaking crests, with  $k < d \cdot k_B$ , where  $d \gg 1$  is a dividing parameter; in order to be consistent with TSM estimates, it is specified here as  $d = 3\text{--}4$  [36]. However, quasi-specular facets do not provide cross-polarized scattering. Therefore, we assume that CPwb is governed by quasi-resonant scattering from small-scale breaking crest roughness, around  $k = k_B$ .

Indeed, a breaking wave crest generates enhanced isotropic surface roughness with a totally saturated spectrum  $\propto k^{-4}$  confined to the localized breaking zone [37]. A local spectrum of this roughness will peak at a wave number,  $k_p$ , linked to the wave breaking wavenumber,  $k_{wb}$ , defined as  $k_p = pk_{wb}$ , with the parameter  $p$  varying from 5 to 10. This scale of breaking crests roughness,  $k_p$ , imposes the range of breaking waves, providing the CPwb- and NP-signals. For the CPwb signal, the range of breaking waves is:  $k_{wb} < k_{CP} \equiv k_B/p$ , and for NP is:  $k_{wb} < k_{NP} \equiv k_B/(pd)$ . Thus, the breaking waves contributing to NP are *longer* than those contributing to CP.

Following [17] (see also Equations (11) and (13) from [24]), both NP and CPwb are proportional to the fraction of the ocean surface covered by the breaking zone

$$q_{wb} \propto \iint_{k < k_{wb}} \beta Bd\varphi d\ln k \propto c_\beta \left( u_*^2 k_{wb} / g \right)^{1+1/n_g} \quad (5)$$

where  $\beta = C_\beta (u_*/c)^2$  is the wind wave growth rate and  $C_\beta$  is a constant in the range  $C_\beta = (2 - 4) \times 10^{-2}$ ,  $B$  is saturation spectrum of wind waves,  $k_{wb}$  is the upper limit of the breaking waves range, equal to  $k_{wb} = k_{NP}$  or  $k_{wb} = k_{CP}$  for NP and CP, respectively. To derive the second relation, we used the fact that the integral is converged at the upper limit, and that in the equilibrium range  $B \propto (u_*/c)^{2/n_g}$  where  $n_g$  is a parameter of the wave breaking dissipation, ranging from  $n_g = 2$  [38] to  $n_g = 5$  [9,39]. According to [31], the wind exponent of CPwb is about 2.4, corresponding to parameter  $n_g = 5$ .

To evaluate modulations of PD-, NP-, and CPwb-signals by the currents we define the relaxation scales of the scattering elements as (see [17] for more details),

$$\tau = m_*/(2\beta) \quad (6)$$

where  $\tau$  is relaxation time scaled by the wave frequency,  $m_*$  is the wind exponent of the wave spectrum. Correspondingly, the relaxation scale length  $kl = (1/2)\tau$  is

$$kl = c_r m_* (g/ku_{10}^2) \quad (7)$$

where  $c_r = (4c_\beta C_D)^{-1} \propto 5 \times 10^3$  is the overall relaxation scale constant.

We then consider wavenumbers  $k_B$ ,  $k_{CP}$ , and  $k_{NP}$  as typical scales for the scatter for PD, CPwb, and NP, correspondingly. For the Bragg waves (with  $k$  around  $10^2$  rad/m for C-band) and  $m_*$  around 1 (see Figure 12 from [31]), the relaxation scale for wind speed from  $u_{10} = 3$  m/s to  $u_{10} = 10$  m/s varies in the range given by  $l_{PD} = 0.05$ – $0.5$  m. Since  $l_{CP} = m_* P^2 l_{PD}$  and  $l_{NP} = m_* P^2 d^2 l_{PD}$  (with  $m_* = 2/n_g = 0.4$ ), the relaxation length scales for CPwb and NP scatterers varies in the range from  $l_{CP} = 0.4$  m to  $l_{CP} = 4$  m, and where  $l_{NP} = 1$  m varying to 100 m, correspondingly. From these rather short relaxation scales, we anticipate that PD, CRwb and NP should follow wind speed variations on spatial scales exceeding 100 meters. This is in line with observations shown in Figure 1, where wind speed oscillations caused by atmospheric gravity waves lead to coherent oscillatory features for any quad-polarized scattering combinations.

Considering current non-uniformities on a scale,  $L$ , from hundred meters to kilometers, condition  $L > (l_{PD}, l_{CP}, l_{NP})$  is also fulfilled. The modulation transfer function (MTF),  $T(k) = \tilde{B}/B_0$ , for the wave spectrum can be expressed as (see [10,17])

$$T(k) = \tau \omega^{-1} m_k \cos^2 \varphi \cdot \text{div}(u) \quad (8)$$

where  $m_k$  is the wavenumber exponent of the wave action spectrum,  $m_k \approx -9/2$ ,  $\varphi$  is wavenumber direction relative to the wind, and  $\text{div}(u)$  is the local divergence of the surface current. Indeed, among the different components of the current velocity gradient tensor, the divergence provides the main contribution to modulation of any ocean surface quantities integrated over the azimuth (like the total mean square slopes, or the total fraction of the wave breaking area defined by Equation (5)). Referring to Equation (8) with (6), one finds that the expected modulation of the Bragg wave spectrum by an ocean current with gradient of order  $10^{-3}$  is negligible. This is consistent with observations, confirming that short scale Bragg waves do not “feel” the current (see Figures 3, 9 and 11). However, due to small relaxation scale, PD-signals follow any variations of the near-surface wind speed (Figures 1d and 5d).

Unlike PD, modulations of NP and CP signals depend on the impact of surface currents over a rather wide spectral range, forming  $q_{wb}$  as defined by (5). As mentioned above, relaxation scales for the upper limits of the integrals in Equation (5),  $k_{NP}$  and  $k_{CP}$ , are of order 100 m. Therefore, spectral modulations at these upper limits due to the currents are expected to be small and to be governed by the wind speed modulations/changes. Yet, current-induced modulations of the longer wave components (forming  $q_{wb}$ ) due to larger relaxation scales can be significant. Although these longer components do not likely provide dominant contributions to background (no currents) NP and CP signal values, their impacts on current-induced modulations of these signals can be significant.

An approximate solution for the modulation of wave breaking by the current can be taken from ([10], their Equation (7)). However, this solution was derived for the Phillips (1985) spectrum [38] with parameter  $n_g$  in Equation (5) equal to  $n_g = 2$  which differs from the one adopted here ( $n_g = 5$ ). Therefore, to assess wave breaking modulations by the currents in the present study, we use the

asymptotic form of the MTF (Equation (8)). This gives the following expression for the expected modulations of the ocean surface area covered by breaking zones:

$$\tilde{q}_{wb} = (n_g + 1) \operatorname{div}(u) \int_{k < k_{wb}^R} \int T(k, \varphi) \beta B(k, \varphi) d\varphi dk \approx 2m_k \omega_p^{-1} \operatorname{div}(u) \quad (9)$$

where  $\omega_p$  is the spectral peak frequency of the wind waves:  $\omega_p \approx g/u_{10}$ , and the approximate relationship is valid for  $n_g \gg 1$ . As previously discussed, although longer breaking waves provide rather weak overall contributions to NP and CPwb signals, their contributions to radar scattering modulations (due to larger relaxation scales) can be significant. Notice that Equation (9) is similar to a previously derived expression ([10], their Equation (7)); both are proportional to  $(u_{10}/g)\operatorname{div}(u)$ . However, the proportionality constant in the previously derived expression is weakly dependent on the scale of the currents and the wind speed.

Using Equations (5) and (9), the current-induced contrasts of NP- and CPwb-signals can be evaluated as:

$$K_{wb} \propto \left( \frac{2m_k}{c_\beta} \right) \frac{g}{u_*^2 k_{wb}} \omega_p^{-1} \operatorname{div}(u) \text{ or } K_{wb} \propto c_r (u_{10} k_{wb})^{-1} \operatorname{div}(u) \quad (10)$$

where  $c_r = 2m_k/(c_\beta C_D) \sim 2 \times 10^5$ ,  $C_D$  is the drag coefficient, subscript 'wb' should be replaced by 'CP' or 'NP', to represent cross-polarized or non-polarized signals, respectively.

Relationship (10) states that although the SAR signal will detect the areas of the surface current convergence, the SAR contrasts will decrease with increasing wind speed. As predicted by (10), the magnitude of the contrast is also dependent on the ability of the shortest breaking wave scales to support one or other scattering mechanism. As already discussed, the upper limit,  $k_{wb}$ , of wave breaking contributing to CP, is equal to:  $k_{wb} \rightarrow k_{CP} = k_B/p$ , and for NP is:  $k_{wb} \rightarrow k_{NP} = k_B/(pd)$ . Thus, current-induced contrasts in the CPwb-signals are suggested to be less than those in NP signals:

$$K_{CP}/K_{NP} = d^{-1} \quad (11)$$

Considering that  $d$  is in the range  $d = 3\text{--}4$ , the ratio between the contrasts is expected to lie in the range from 0.24 to 0.3, as is approximately reported (see Table 2).

## 5. Conclusions

Using the approach suggested in [24,29] as applied to a set of C-band quad-polarized SAR images, we have investigated SAR imaging mechanisms of the ocean currents. Analysis of the data confirms that the governing mechanism that leads to a manifestation of ocean current features in quad-polarized SAR images is wave breaking modulations by the currents. In contrast to short resonant Bragg scatters, breaking waves are very sensitive to surface current gradients. As interpreted, the relaxation scale of C-band Bragg waves is of order 1 m which is much smaller than current scales, and thus Bragg scattering from a regular (non-breaking) ocean surface is not relevant to radar imaging of the ocean currents, with respect to both co- and cross-polarizations.

Non-polarized radar returns from large-scale elements of breaking wave crests, and resonant cross-polarized scattering from the roughness of small-scale breaking crests, significantly contribute to the dual co-polarized and cross-polarized NRCS of the ocean surface [31]. As found, strong sensitivity of wave breaking to the presence of the surface current gradients leads to quite well detectable current signatures in both co- and cross-polarized SAR images. More remarkably, the current-induced contrasts of the *non*-polarized returns from breaking waves are found to largely exceed, by a factor of about 3, the contrasts of the *cross*-polarized scattering from breaking waves. A possible reason lies in the distinct co- and cross-polarized scattering mechanisms from breaking waves. For the former, quasi-specular radar returns dominate, while for the latter, quasi-resonant scattering from rough breaking crests governs the backscatter intensity. The differing sensitivity then relates to distinct spectral intervals of breaking waves supporting quasi-specular returns (non-polarized), and cross-polarized

quasi-resonant scattering. Accordingly, routinely observed current signatures in quad-polarized SAR images essentially originate from wave breaking modulations, and polarized contrast sensitivity can further help quantitatively retrieve the strength of surface current gradients.

Future investigations will capitalize on the proposed methodology to exploit similar decomposition to analyze Doppler shifts [5,6]. This approach will help more consistently separate the surface currents and the wave-induced impacts from the measured polarized Doppler shifts.

**Author Contributions:** V.K., B.Z. and B.C. conceived the original idea of the study, suggested for the topic, and contributed to the interpretation of the results; S.F. carried out the RADARSAT-2 data analysis and prepared all of the figures; B.C., W.P. and A.M. assisted in manuscript revision. S.F., V.K. and B.Z. wrote the manuscript.

**Funding:** This research received no external funding other than what is acknowledging below.

**Acknowledgments:** S.F. and B.Z. acknowledge support of National Key Research and Development Program of China under Grant 2016YFC1401001, National Science Foundation of China for Outstanding Young Scientist under Grant 41622604, the Excellent Youth Science Foundation of Jiangsu Province under Grant BK20160090, the National Program on Global Change and Air–Sea Interaction (GASI-IPOVAI-04), and the International Cooperation, CAS, Chinese–Foreign Cooperation in Key Project under Grant 133337KYSB20160002. V.K. and B.C. acknowledge support of Russian Science Foundation project no. 17-77-30019. W.P. acknowledges support from the Canadian Space Agency under SWOT, the Surface Water Ocean Topography program, and GRIP, the Government Research Initiative Program.

**Conflicts of Interest:** The authors declare no conflict of interest.

## References

1. Lumpkin, R.; Pazos, M. Measuring surface currents with Surface Velocity Program drifters: The instrument, its data, and some recent results. In *Lagrangian Analysis and Prediction of Coastal and Ocean Dynamics*; Cambridge University Press: Cambridge, UK, 2007; pp. 39–67.
2. Lund, B.; Gruber, H.C.; Hessner, K.; Williams, N.J. On shipboard marine X-band radar near-surface current “calibration”. *J. Atmos. Ocean. Technol.* **2015**, *32*, 1928–1944. [[CrossRef](#)]
3. Weber, B.L.; Barrick, D.E. On the nonlinear theory for gravity waves on the ocean’s surface: Part I. Derivations. *J. Phys. Oceanogr.* **1977**, *7*, 3–10. [[CrossRef](#)]
4. Broche, P.; Maistre, J.C.; Forget, P. Measure par radar de ‘came’trique cohérent des courants superficiels engendrés par le vent. *Oceanol. Acta* **1983**, *6*, 43–53.
5. Chapron, B.; Collard, F.; Ardhuin, F. Direct measurements of ocean surface velocity from space: Interpretation and validation. *J. Geophys. Res. Oceans* **2005**, *110*, 1–17. [[CrossRef](#)]
6. Johannessen, J.A.; Chapron, B.; Collard, F.; Kudryavtsev, V.; Mouche, A.; Akimov, D.; Dagestad, K.-F. Direct ocean surface velocity measurements from space: Improved quantitative interpretation of Envisat ASAR observations. *Geophys. Res. Lett.* **2008**, *35*, 1–6. [[CrossRef](#)]
7. Romeiser, R.; Suchandt, S.; Runge, H.; Steinbrecher, U.; Grüner, S. First analysis of TerraSAR-X along-track InSAR-derived current fields. *IEEE Trans. Geosci. Remote Sens.* **2010**, *48*, 820–829. [[CrossRef](#)]
8. Romeiser, R.; Runge, H.; Suchandt, S.; Kahle, R.; Rossi, C.; Bell, P.S. Quality assessment of surface current fields from TerraSAR-X and TanDEM-X along-track interferometry and doppler centroid analysis. *IEEE Trans. Geosci. Remote Sens.* **2014**, *52*, 2759–2772. [[CrossRef](#)]
9. Kudryavtsev, V.; Myasoedov, A.; Chapron, B.; Johannessen, J.A.; Collard, F. Joint sun-glitter and radar imagery of surface slicks. *Remote Sens. Environ.* **2012**, *120*, 123–132. [[CrossRef](#)]
10. Kudryavtsev, V.; Myasoedov, A.; Chapron, B.; Johannessen, J.; Collard, F. Imaging meso-scale upper ocean dynamics using SAR and optical data. *J. Geophys. Res. Oceans* **2012**, *117*, 1–13. [[CrossRef](#)]
11. Alpers, W.; Hennings, I. A theory of the imaging mechanism of underwater bottom topography by real and synthetic aperture radar. *J. Geophys. Res. Oceans* **1984**, *89*, 10529–10546. [[CrossRef](#)]
12. Holliday, D.; St-Cyr, G.; Woods, N.E. A radar ocean imaging model for small to moderate incidence angles. *Int. J. Remote Sens.* **1986**, *7*, 1809–1834. [[CrossRef](#)]
13. Lyzenga, D.R.; Bennett, J.R. Full-spectrum modeling of synthetic aperture radar internal wave signatures. *J. Geophys. Res. Oceans* **1988**, *93*, 12345–12354. [[CrossRef](#)]
14. Thompson, D.R. Calculation of radar backscatter modulations from internal waves. *J. Geophys. Res. Oceans* **1988**, *93*, 12371–12380. [[CrossRef](#)]

15. Romeiser, R.; Alpers, W. An improved composite surface model for the radar backscattering cross section of the ocean surface: 2. Model response to surface roughness variations and the radar imaging of underwater bottom topography. *J. Geophys. Res. Oceans* **1997**, *102*, 25251–25267. [[CrossRef](#)]
16. Cooper, A.L.; Chubb, S.R.; Askari, F.; Valenzuela, G.R.; Keller, W.C.; Bennett, J.R. Radar surface signatures for the two-dimensional tidal circulation over Phelps Bank, Nantucket shoals: A comparison between theory and experiment. *J. Geophys. Res. Oceans* **1994**, *99*, 7865–7883. [[CrossRef](#)]
17. Kudryavtsev, V.; Akimov, D.; Johannessen, J.; Chapron, B. On radar imaging of current features: 1. Model and comparison with observations. *J. Geophys. Res. Oceans* **2005**, *110*, 1–27. [[CrossRef](#)]
18. Lyzenga, D.R. Effects of Wave Breaking on Sar Signatures Observed Near the Edge of the Gulf Stream. In Proceedings of the International Geoscience & Remote Sensing Symposium, Lincoln, NE, USA, 31 May 1996.
19. Wetzel, L.B. *On Microwave Scattering by Breaking Waves, in Wave Dynamics and Radio Probing of the Ocean Surface*; Phillips, O.M., Hasselmann, K., Eds.; Springer: New York, NY, USA, 1986; pp. 273–284.
20. Chubb, S.; Cooper, A.; Jansen, R.; Fusina, R.; Askari, F.; Lee, J.-S. Radar backscatter from breaking waves in Gulf Stream current convergence fronts. *IEEE Trans. Geosci. Remote Sens.* **1999**, *37*, 1951–1966. [[CrossRef](#)]
21. Jansen, R.W.; Shen, C.Y.; Chubb, S.R.; Cooper, A.L.; Evans, T.E. Subsurface, surface, and radar modeling of a Gulf Stream current convergence. *J. Geophys. Res. Oceans* **1998**, *103*, 18723–18743. [[CrossRef](#)]
22. Snyder, R.L.; Kennedy, R.M. On the formation of whitecaps by a threshold mechanism: 1. Basic formation. *J. Phys. Oceanogr.* **1983**, *13*, 1482–1492. [[CrossRef](#)]
23. Hughes, B.A. The effect of internal waves on surface wind waves: 2. Theoretical analysis. *J. Geophys. Res. Oceans* **1978**, *83*, 455–465. [[CrossRef](#)]
24. Kudryavtsev, V.; Kozlov, I.; Chapron, B.; Johannessen, J.A. Quad-polarization SAR features of ocean currents. *J. Geophys. Res. Oceans* **2014**, *119*, 6046–6065. [[CrossRef](#)]
25. Zhang, G.; Perrie, W. Dual-Polarized Backscatter Features of Surface Currents in the Open Ocean during Typhoon Lan (2017). *Remote Sens.* **2018**, *10*, 875. [[CrossRef](#)]
26. Kudryavtsev, V.; He, Y.; Zhang, B.; Liu, G.; Hu, H.; Perrie, W.; Shen, H. Radar imaging of intense nonlinear Ekman divergence. *Geophys. Res. Lett.* **2016**, *43*, 9810–9818.
27. Jones, C.T.; Sikora, T.D.; Vachon, P.W.; Buckley, J.R. Ocean feature analysis using automated detection and classification of sea-surface temperature front signatures in RADARSAT-2 images. *Bull. Am. Meteorol. Soc.* **2014**, *95*, 677–679. [[CrossRef](#)]
28. Kudryavtsev, V.; Hauser, D.; Caudal, G.; Chapron, B. A semiempirical model of the normalized radar cross-section of the sea surface 1. Background model. *J. Geophys. Res. Oceans* **2003**, *108*, 1–24. [[CrossRef](#)]
29. Kudryavtsev, V.N.; Chapron, B.; Myasoedov, A.G.; Collard, F.; Johannessen, J.A. On Dual Co-Polarized SAR Measurements of the Ocean Surface. *IEEE Geosci. Remote Sens. Lett.* **2013**, *10*, 761–765. [[CrossRef](#)]
30. Hansen, M.W.; Kudryavtsev, V.; Chapron, B.; Brekke, C.; Johannessen, J.A. Wave Breaking in Slicks: Impacts on C-Band Quad-Polarized SAR Measurements. *IEEE J. Sel. Top. Appl. Earth Obs. Remote Sens.* **2016**, *9*, 1–12. [[CrossRef](#)]
31. Kudryavtsev, V.N.; Fan, S.; Zhang, B.; Mouche, A.A.; Chapron, B. On Quad-Polarized SAR Measurements of the Ocean Surface. *IEEE Trans. Geosci. Remote Sens.* **2019**, *1*–9. [[CrossRef](#)]
32. Slade, B. RADARSAT-2 Product Description. Issue 1/6, RN-SP-52-1238. Available online: [http://gsmdacorporation.com/products/sensor/radarsat2/RS2\\_Product\\_Description.pdf](http://gsmdacorporation.com/products/sensor/radarsat2/RS2_Product_Description.pdf) (accessed on 1 January 2018).
33. Lu, Y.; Zhang, B.; Perrie, W.; Mouche, A.A.; Li, X.; Wang, H. A C-Band Geophysical Model Function for Determining Coastal Wind Speed Using Synthetic Aperture Radar. *IEEE J. Sel. Top. Appl. Earth Obs. Remote Sens.* **2018**, *11*, 2417–2428. [[CrossRef](#)]
34. Beal, R.; Kudryavtsev, V.; Thompson, D.; Grodsky, S.; Tilley, D.; Dulov, V.; Gruber, H. The influence of the marine atmospheric boundary layer on ERS-1 synthetic aperture radar imagery of the Gulf Stream. *J. Geophys. Res. Oceans* **1997**, *102*, 5799–5814. [[CrossRef](#)]
35. Kuang, H.-L.; Perrie, W.; Xie, T.; Zhang, B.; Chen, W. Retrievals of sea surface temperature fronts from SAR imagery. *Geophys. Res. Lett.* **2012**, *39*, 1–7. [[CrossRef](#)]
36. Voronovich, A.G.; Zavorotny, V.U. Theoretical model for scattering of radar signals in Ku- and C-bands from a rough sea surface with breaking waves. *Waves Random Media* **2001**, *11*, 247–269. [[CrossRef](#)]
37. Walker, D.T.; Lyzenga, D.R.; Ericson, E.; Lung, D.E. Radar backscatter and surface roughness measurements from stationary breaking waves. *Philos. Trans. R. Soc. Lond. Ser. A* **1996**, *351*, 1953–1984.

38. Phillips, O.M. Spectral and statistical properties of the equilibrium range in wind-generated gravity waves. *J. Fluid Mech.* **1985**, *156*, 505–531. [[CrossRef](#)]
39. Yurovskaya, M.V.; Dulov, V.A.; Chapron, B.; Kudryavtsev, V.N.; Yurovskaya, M.; Dulov, V. Directional short wind wave spectra derived from the sea surface photography. *J. Geophys. Res. Oceans* **2013**, *118*, 4380–4394. [[CrossRef](#)]



© 2019 by the authors. Licensee MDPI, Basel, Switzerland. This article is an open access article distributed under the terms and conditions of the Creative Commons Attribution (CC BY) license (<http://creativecommons.org/licenses/by/4.0/>).